Chinese Chemical Letters 36 (2025) 110467

Contents lists available at ScienceDirect

Chinese Chemical Letters

journal homepage: www.elsevier.com/locate/cclet

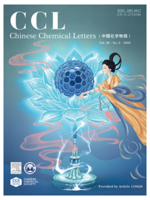

Structuring MoO_3-polyoxometalate hybrid superstructures to boost electrocatalytic hydrogen evolution reaction

Bowen Li, Ting Wang*, Ming Xu, Yuqi Wang, Zhaoxing Li, Mei Liu*, Wenjing Zhang, Ming Feng*

Key Laboratory of Functional Materials Physics and Chemistry of the Ministry of Education, Jilin Normal University, Changchun 130103, China

ARTICLE INFO

Article history:
Received 26 June 2024
Revised 12 September 2024
Accepted 14 September 2024
Available online 15 September 2024

Keywords:
Polyoxometalate
Metal oxide
Electrocatalysis
Superstructure
Hydrogen production

ABSTRACT

Improving the surface atoms utilization efficiency of catalysts is extremely important for large-scale H_2 production by electrochemical water splitting, but it remains a great challenge. Herein, we reported two kinds of MoO_3-polyoxometalate hybrid nanobelt superstructures (MoO_3-POM HNSs, POM = $PW_{12}O_{40}$ and $SiW_{12}O_{40}$) using a simple hydrothermal method. Such superstructure with highly uniform nanoparticles as building blocks can expose more surface atoms and emanate increased specific surface area. The incorporated POMs generated abundant oxygen vacancies, improved the electronic mobility, and modulated the surface electronic structure of MoO_3, allowing to optimize the H^* adsorption/desorption and dehydrogenation kinetics of catalyst. Notably, the as-prepared MoO_3-$PW_{12}O_{40}$ HNSs electrodes not only displayed the low overpotentials of 108 mV at 10 mA/cm^2 current density in 0.5 mol/L H_2SO_4 electrolyte but also displayed excellent long-term stability. The hydrogen evolution reaction (HER) performance of MoO_3-POM superstructures is significantly better than that of corresponding bulk materials $MoO_3@PW_{12}O_{40}$ and $MoO_3@SiW_{12}O_{40}$, and the overpotentials are about 8.3 and 4.9 times lower than that of single MoO_3. This work opens an avenue for designing highly surface-exposed catalysts for electrocatalytic H_2 production and other electrochemical applications.

Rapid consumption of fossil fuels has exposed clear deficiencies in future energy and environmental, thus exploring clean and renewable energy for sustainable development is extremely important [1–5]. Owing to its eco-friendly and reproducible properties, hydrogen is perceived as a promising alternative to traditional fossil fuels [6,7]. Compared to traditional technologies, hydrogen production through electrocatalytic water splitting has become a prospective and effective strategy due to its high energy-conversion efficiency [8,9]. Nevertheless, the sluggish reaction kinetics of hydrogen evolution reaction (HER) generally leads to large extra energy consumption [10,11]. To mitigate the reaction energy barriers and accelerate the reaction dynamics, advanced catalysts require to be developed [12,13]. Although precious metal Pt-based material has been shown to be the most efficient catalyst for HER, the exorbitant price and scarcity still restrict its large-scale applications [14,15]. Therefore, it is necessary to explore highly active, cost-effective, and durable noble metal-free HER electrocatalysts to achieve the economic production of hydrogen.

Recently, transition metal derivatives such as oxides, phosphides, carbides, and chalcogenides have been exploited as potential substitutes due to their excellent electrochemical properties [16–19]. Among various transition metal oxides, molybdenum oxide (MoO_3) has attracted much attention because of its special electronic and unique stable orthorhombic structure, which can enable it to build high-quality electronic interface. Several approaches have been proposed to design the MoO_3-based materials to achieve the enhanced catalytic activity, such as doping elements, vacancy engineering, introducing heterointerfaces, and coupling with conductive carbon supports [20–23]. For example, Xu *et al.* reported a petal-shaped two-dimensional MoO_3 nanosheets confining Pd nanoparticles (Pd@MoO_3), which only require a low overpotential of 71 mV to maintain the 10 mA/cm^2 for HER in acidic electrolyte [24]. Hu *et al.* presented an efficient amorphous NiO nanosheets coupled with ultrafine Ni and MoO_3 nanoparticles (MoO_3/Ni-NiO) with two heterostructures, which only require a low overpotential of 62 mV at 10 mA/cm^2, outperforming many materials previously reported [25]. Although great efforts have been made, the addition of noble metal and poor conductivity, as well as lack of large number of active sites still restrict its further large-scale usage.

---

* Corresponding authors.
E-mail addresses: wangt@jlnu.edu.cn (T. Wang), liumei@jlnu.edu.cn (M. Liu), mingfeng@jlnu.edu.cn (M. Feng).

https://doi.org/10.1016/j.cclet.2024.110467

Size effect plays a significant role in nanomaterials. When the size of nanomaterials reduces, the exposure of surface atoms and specific surface area of materials will show a sharp increase [26]. Superstructures with highly uniform nanoparticles as building blocks have gained intensive attention since the photoelectric characteristics are not only determined by the individual nanoparticle, but also by the optical and electronic communication between these nanoparticles [27]. Therefore, the engineering of multi-component MoO_3-based hybrid superstructures become a promising avenue to improve the electrocatalytic performance due to the possible potential synergetic effect and size-induced new physical and chemical properties. In this regard, polyoxometalates (POMs) is one type of promising functional components to improve the electrocatalytic property because of the unique nanostructure and electrochemical characteristics such as high structure/thermal stability, proton and electron transfer/storage abilities, as well as the instability of its lattice oxygen [28–30]. A large number of POMs have been employed to construct heterostructure hybrid catalysts for HER. For example, Yang *et al.* reported an effective heterostructure of POM nanoplates and zinc iron oxide (P_2Mo_{18}-$ZnFe_2O_4$), which exhibit excellent HER performance with the low overpotentials of 268 and 356 mV to achieve 20 and 50 mA/cm^2 [31]. Wei *et al.* using POMs anchored zinc cobalt sulfide nanowire on Ni-foam (PW_{12}@ZnCoS/NF) for HER, remarkable activity was achieved at a low overpotential of 170 and 330 mV, giving the 20 and 50 mA/cm^2 [32].

Thought-provoking, if we combine MoO_3 with POMs to construct a superstructure hybrid nanomaterial, the unexpected catalytic performance may bring about. Concerned about all this, two hybrid nanobelt superstructures (MoO_3-$PW_{12}O_{40}$ HNSs and MoO_3-$SiW_{12}O_{40}$ HNSs) were synthesized using a simple hydrothermal method *via* introducing two type of POM clusters into MoO_3 system during the nucleation stage. Detailed analyses reveal that the incorporated POMs can generate abundant oxygen vacancies and achieve higher electronic mobility. Meanwhile, the incorporation of POMs can provide larger specific surface area, expose more active sites, and modulate the surface electronic structure, thus enhancing the HER performance. Thanks to the induced physical/chemical properties and synergistic effect among various components, MoO_3-$PW_{12}O_{40}$ HNSs and MoO_3-$SiW_{12}O_{40}$ HNSs deliver the excellent HER behavior, exhibiting the overpotentials of 108 and 183 mV at 10 mA/cm^2, with the Tafel slopes of 67.6 and 91.6 mV/dec in 0.5 mol/L H_2SO_4 electrolyte. Their overpotentials are significantly lower than that of corresponding MoO_3@$PW_{12}O_{40}$ (352 mV) and MoO_3@$SiW_{12}O_{40}$ (380 mV), and about 8.3 and 4.9 times lower than that of MoO_3.

The synthesis process of the MoO_3-POM HNSs is illustrated in Fig. 1a, in which two types of POM clusters were introduced to the MoO_3 matrix at the nucleation stage. The morphology and structure of MoO_3-$PW_{12}O_{40}$ and MoO_3-$SiW_{12}O_{40}$ HNSs were characterized by scanning electron microscope (SEM), transmission electron microscope (TEM) and X-ray diffraction (XRD). The SEM images (Fig. 1b and Fig. S1 in Supporting information) show that although the employed tungsten-based POM clusters are different, the same morphologies of the products can be observed. The TEM images indicate that plenty of well-distributed 1D thin nanobelts with the thickness about 10 nm were formed (Figs. 1c and d). And we found that the structure of such hybrid nanobelts were highly ordered. The interplanar spacing was measured to be 0.39 nm, which was assigned to the (011) planes of MoO_3 (Fig. 1e) [33]. Meanwhile, it proved that many monodisperse POM particles marked with red circles were incorporated into MoO_3 in an orderly fashion and created abundant defects. The elemental mappings (Fig. 1f) illustrate the uniform distribution of Mo, O, W, and P throughout the HNSs. The Mo, O, W, P, and Si elemental content are confirmed by energy dispersive X-ray spectroscopy (EDX) and summarized in Table S1 (Supporting information).

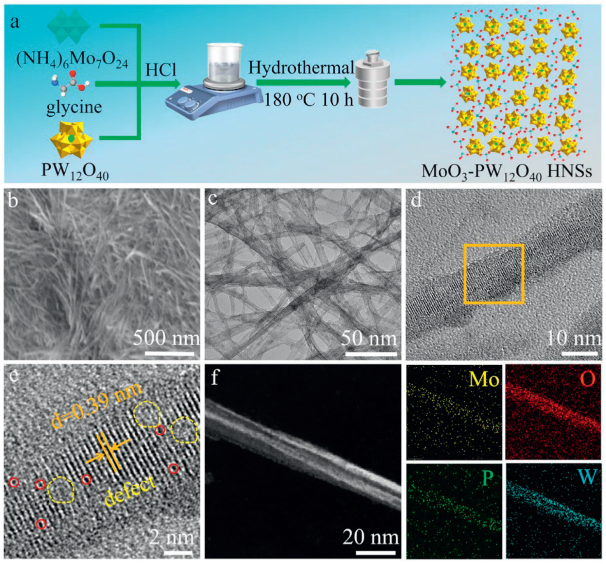

Fig. 1. (a) Synthesis process schematic of MoO_3-POM HNSs. (b) SEM image, (c) TEM and (d, e) HRTEM images of MoO_3-$PW_{12}O_{40}$ HNSs. (f) Elemental mappings of Mo, O, P, and W in MoO_3-$PW_{12}O_{40}$ HNSs.

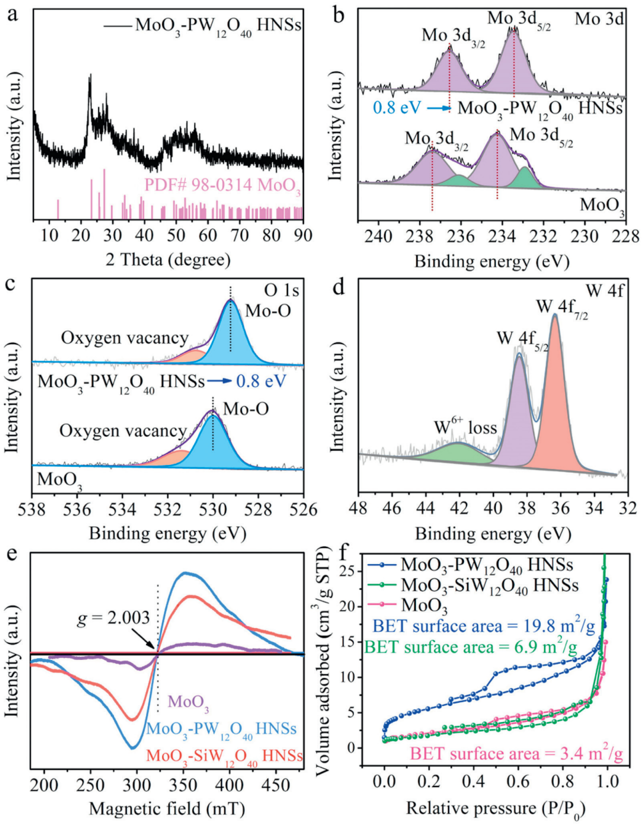

Fig. 2. (a) XRD patterns of MoO_3-$PW_{12}O_{40}$ HNSs. (b) Mo 3d, (c) O 1s, and (d) W 4f XPS spectrum of MoO_3-$PW_{12}O_{40}$ HNSs and MoO_3. (e) The EPR spectrum and (f) N_2 adsorption-desorption isotherms of different catalysts.

Fig. 2a shows the XRD pattern of MoO_3-$PW_{12}O_{40}$ HNSs, which is in accordance with the MoO_3 phase (PDF#98–0314). The obvious diffraction peaks located at 23.3°, 25.7°, 27.3°, 46.2° and56.2° are assigned to the (110), (040), (021), (210), and (231) crystal planes. While no characteristic peaks related to POM are present in the composite, which may be attributed to the low content and formation of dispersive POM clusters, rather than aggregated large crystals [34,35]. Such similar result can also be observed for MoO_3-$SiW_{12}O_{40}$ HNSs (Fig. S4 in Supporting information). Fourier transform infrared (FTIR) spectroscopy presented in Fig. S5 (Supporting information) offers extremely powerful evidence for the formation of hybrids since both the characteristic peaks of MoO_3 and POM present in the MoO_3-POM HNSs. The TGA data (Fig. S6 in Supporting information) demonstrates that the MoO_3-$PW_{12}O_{40}$ HNSs can keep stable when temperature is lower than 600 °C and the estimated $PW_{12}O_{40}$ content in the composite is approximately 50.6 wt% [36]. The elemental composition and valence states of MoO_3-$PW_{12}O_{40}$ HNSs and MoO_3 are analyzed by the X-ray photoelectron spectroscopy (XPS). The full XPS spectra demonstrate the existence of Mo and O elements in MoO_3, and Mo, O, W elements for MoO_3-$PW_{12}O_{40}$ HNSs (Fig. S7 in Supporting information). The high-resolution XPS spectra of Mo 3d demonstrate that both Mo^{5+} and Mo^{6+} species can be detected from MoO_3 (Fig. 2b), two green-filled fitted peaks located at the binding energies of 232.9 eV and 236.1 eV are derived from Mo $3d_{5/2}$ and Mo $3d_{3/2}$ of Mo^{5+}, and the other two purple-filled fitted peaks located at the binding energies of 234.3 eV and 237.4 eV originate from Mo $3d_{5/2}$ and Mo $3d_{3/2}$ of Mo^{6+}, which demonstrates the generation of MoO_3 phase. Compared to MoO_3, the fitted peaks associated with Mo^{5+} in MoO_3-$PW_{12}O_{40}$ HNSs disappear, and the position of the Mo^{6+} species is negatively shifted by 0.8 eV [37]. The O 1s spectra is also provided as Fig. 2c. The binding energies at 530.0 eV and 531.3 eV in MoO_3 are assigned to Mo-O and oxygen vacancy, respectively [38]. The position of the Mo-O in MoO_3-$PW_{12}O_{40}$ HNSs is also negatively shifted by 0.8 eV. The intrinsic charge differences can be resultant from the electron interactions between different species, *i.e.* the electron transfer from POM to MoO_3 [39]. In the W 4f spectrum (Fig. 2d), the orange- and purple-filled fitted peaks located at the binding energies of 36.2 eV and 38.4 eV are attributed to the W $4f_{7/2}$ and W $4f_{5/2}$ of W^{6+}, respectively, confirming the existence of POM in the composite [40]. Moreover, the electron paramagnetic resonance (EPR) spectra of MoO_3 and MoO_3-$PW_{12}O_{40}$ HNSs were carried out. As demonstrated in Fig. 2e, all the samples exhibited apparent characteristic signal at $g = 2.003$, and the corresponding signals are significantly enhanced after forming MoO_3-POM hybrid superstructures, which corroborated the introduction of oxygen vacancies into the MoO_3 by introducing the POM into MoO_3 system and is consistent with the TEM result [41]. We further synthesized two comparative samples (MoO_3@$PW_{12}O_{40}$ and MoO_3@$SiW_{12}O_{40}$) by adding corresponding POM into the presynthesized MoO_3 precursor system under the same experimental conditions (Fig. S8 in Supporting information). It is observed that the subsequent introduction of POM into the reaction system only led to the formation of aggregated bulks (Fig. S9 in Supporting information), which demonstrated that the formation of MoO_3-POM HNSs can only occur during the nucleation process of MoO_3. Immediately afterwards, N_2 adsorption-desorption isotherms were performed to measure the structural properties of prepared catalysts. As depicted in Fig. 2f, both prepared samples exhibited type IV isotherms, proving the mesoporous properties [42]. The Brunauer-Emmett-Teller (BET) specific surface area of MoO_3-$PW_{12}O_{40}$ HNSs is 19.8 m^2/g, which is significantly higher than MoO_3@$PW_{12}O_{40}$ (6.9 m^2/g) and MoO_3 (3.4 m^2/g). Such larger surface area can offer more catalytic active sites for electrocatalytic reactions and facilitate the contact between the catalyst and electrolyte. Surface wettability of the catalyst has a considerable influence on HER performance. The droplet contacts angle (CA) tests (Fig. S10 in Supporting information) demonstrate that MoO_3-$PW_{12}O_{40}$ HNSs show a smaller CA of 9.76° than MoO_3@$PW_{12}O_{40}$ (28.9°) and MoO_3 (34.04°), proving its super-hydrophilic nature [43]. To better elaborate the electrochemical performance, the Mott-Schottky curves were measured. Fig. S11 (Supporting information) shows that slopes of Mott-Schottky curves are positive, proving the electrons are main carriers. The conduction band of MoO_3-POM HNSs are more negative than MoO_3, which is beneficial to the electron transport during the electrochemical reaction [44].

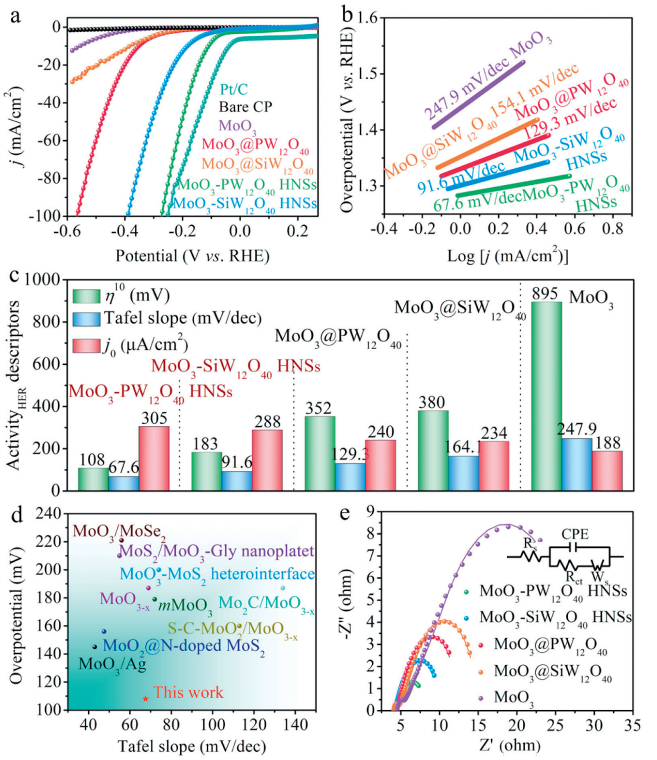

Fig. 3. (a) LSV curves, (b) Tafel slopes, (c) the detailed overpotentials and Tafel values of different catalysts in 0.5 mol/L H_2SO_4. (d) Comparison of overpotentials at 10 mA/cm^2 with other reported similar electrocatalysts. (e) EIS plots of different catalysts in 0.5 mol/L H_2SO_4.

To reveal the distinctive role of superstructures in catalytic reactions, the HER performance of the as-synthesized samples was assessed by linear sweep voltammetry (LSV) in a freshly obtained 0.5 mol/L H_2SO_4 aqueous solution. Fig. 3a shows the LSV curves of prepared samples, bare carbon paper (CP) and commercial Pt/C catalyst. Firstly, the negligible HER activity of CP can be clearly observed through a stable baseline. Among the prepared samples, MoO_3-$PW_{12}O_{40}$ HNSs and MoO_3-$SiW_{12}O_{40}$ HNSs exhibit more impressive HER activity with the lower overpotentials of 108 mV and 183 mV at the current density of 10 mA/cm^2, which are smaller than MoO_3@$PW_{12}O_{40}$ (352 mV), MoO_3@$SiW_{12}O_{40}$ (380 mV), and MoO_3 (895 mV). Even though the HER catalytic activity of MoO_3-$PW_{12}O_{40}$ HNSs is lower than that of commercial Pt/C catalyst at 10 mA/cm^2, it can achieve the comparable performance to benchmark Pt/C at high current densities. The reaction kinetics and mechanism of HER was determined by the Tafel slopes, which are derived from the Tafel equation $\eta = b\log|j| + a$ (Fig. 3b), where "b" is the Tafel slope, "*j*" is the current density, and "a" is the intercept relative to the exchange current density (j_0) [45]. The Tafel slope of MoO_3-$PW_{12}O_{40}$ HNSs and MoO_3-$SiW_{12}O_{40}$ HNSs are 67.6 mV/dec and 91.6 mV/dec, which are smaller than that of MoO_3@$PW_{12}O_{40}$ (129.3 mV/dec), MoO_3@$SiW_{12}O_{40}$ (164.1 mV/dec), and MoO_3 (247.9 mV/dec), suggesting the more rapid reaction kinetics at the electrode and electrolyte interface and corresponds to lower overpotentials of MoO_3-$PW_{12}O_{40}$ HNSs and MoO_3-$SiW_{12}O_{40}$ HNSs. Such small Tafel slope implies that the low ac-

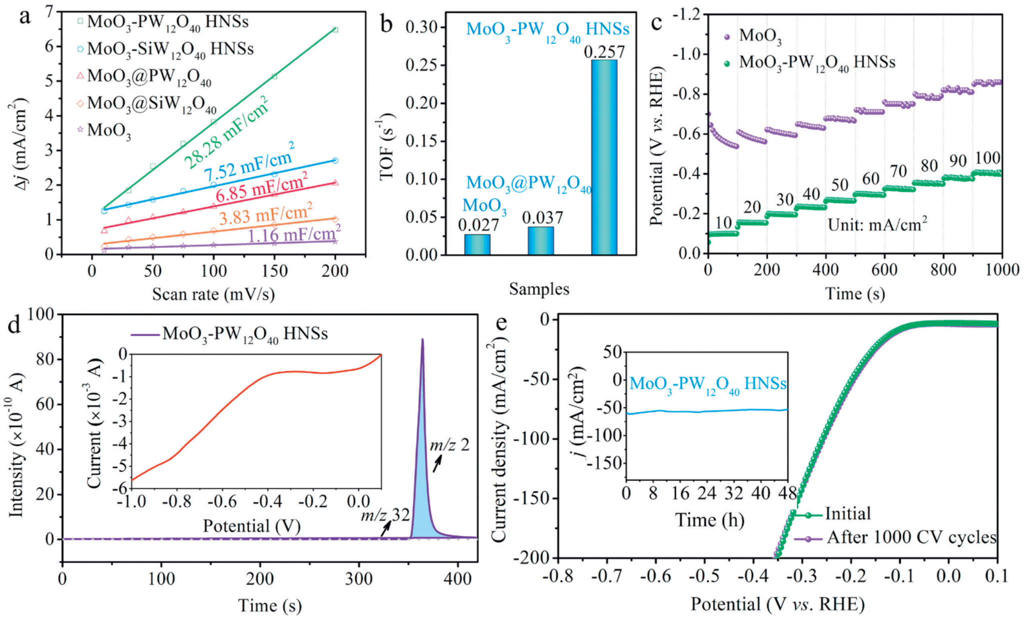

Fig. 4. (a) C_{dl} values of various samples. (b) TOF values of MoO_3, $MoO_3@PW_{12}O_{40}$ and MoO_3-$PW_{12}O_{40}$ HNSs at an overpotential of 100 mV. (c) Multi chronoamperometry comparison of MoO_3-$PW_{12}O_{40}$ HNSs with MoO_3 at current density of 10–100 mA/cm^2 in 0.5 mol/L H_2SO_4 electrolyte. (d) DEMS measurement of MoO_3-$PW_{12}O_{40}$ HNSs (inset: the corresponding *in situ* LSV curve). (e) LSV curves initially and after 1000 CV cycles (inset: the long-term durability tests for 48 h).

tivation energy is required to boost the HER kinetics, and the HER route catalyzed by MoO_3-POM HNSs in acidic electrolyte follows the Volmer-Heyrovsky mechanism [46]. Furthermore, the MoO_3-$PW_{12}O_{40}$ HNSs and MoO_3-$SiW_{12}O_{40}$ HNSs exhibit the exchange current density (j_0) of 305 and 288 μA/cm^2, which are higher than $MoO_3@PW_{12}O_{40}$ (240 μA/cm^2), $MoO_3@SiW_{12}O_{40}$ (234 μA/cm^2), and MoO_3 (188 μA/cm^2), suggesting the superior intrinsic electrocatalytic activity. According to the electrochemical results in Fig. 3c, it can be inferred that the MoO_3-$PW_{12}O_{40}$ HNSs exhibits the ultrahigh activity with the lowest overpotential and Tafel slope, which is better than most previously reported MoO_3-, POM- and other metal oxide-based electrocatalysts, demonstrating its structural and performance advantages (Fig. 3d, Tables S2 and S3 in Supporting information). To gain further insights, electrochemical impedance spectroscopy (EIS) was conducted. The EIS spectra are depicted in Fig. 3e and reveal that MoO_3-POM HNSs possess the lower charge transfer resistance (R_{ct}) than other comparative samples (Table S4 in Supporting information), demonstrating the fast electrochemical reaction kinetics and Faradaic process between the interface of electrolyte and MoO_3-POM HNSs catalysts [47].

The electrochemical active surface area (ECSA) was further estimated from the electrochemical double-layer capacitance (C_{dl}), which was determined by the cyclic voltammetry (CV) curves at different scan rates (Fig. S12 in Supporting information). As revealed in Fig. 4a, the C_{dl} values were calculated to be 28.28, 7.52, 6.85, 3.83, and 1.16 mF/cm^2 for MoO_3-$PW_{12}O_{40}$ HNSs, MoO_3-$SiW_{12}O_{40}$ HNSs, $MoO_3@PW_{12}O_{40}$, $MoO_3@SiW_{12}O_{40}$, and MoO_3, respectively [48]. This indicate the hybrid nanobelt superstructures can expose more active sites in the electrochemical process and trigger the rapid onset of HER. The polarization curves of MoO_3-$PW_{12}O_{40}$ HNSs and MoO_3 were further normalized by ECSA to rule out the effect of surface area on catalytic performance. The ECSA values were obtained by the equation $ECSA = (C_{dl} \times A)/C_s$, where A is the area of working electrode, C_s is the specific capacitance of the sample (0.015 mF/cm^2) [49]. As shown in Fig. S13 (Supporting information), MoO_3-$PW_{12}O_{40}$ HNSs displays the higher specific activity than MoO_3 under the same condition, revealing the enhanced intrinsic activity of MoO_3-$PW_{12}O_{40}$ HNSs than MoO_3 [50]. Additionally, MoO_3-$PW_{12}O_{40}$ HNSs exhibits a turnover frequency (TOF) of 0.257 s^{-1} at an overpotential of 100 mV (Fig. 4b and Fig. S14 in Supporting information), which is a 9.5-fold increase over MoO_3 (0.027 s^{-1}) and higher than $MoO_3@PW_{12}O_{40}$ (0.037 s^{-1}) [51]. Multi chronoamperometry result (Fig. 4c) shows that the voltage at individual current density for MoO_3-$PW_{12}O_{40}$ HNSs is significantly lower than that of MoO_3, demonstrating that MoO_3-$PW_{12}O_{40}$ HNSs possess more excellent mass transport property and electrocatalytic activity than MoO_3.

In the next step, the generated gas during the water electrolysis process was analyzed *via in situ* differential electrochemical mass spectrometry (DEMS). As depicted in Fig. 4d, in parallel with the LSV curve, the H_2 generation can be clearly detected by the online analysis record, but no O_2 signal is observed, suggesting the good selectivity of hydrogen evolution of MoO_3-$PW_{12}O_{40}$ HNSs. It can also be clearly observed that MoO_3-$PW_{12}O_{40}$ HNSs exhibits higher faradaic ion current than that of MoO_3 (Fig. S15 in Supporting information). Moreover, the amount of collected H_2 for MoO_3-$PW_{12}O_{40}$ HNSs is larger than that of MoO_3 and match well with the theoretically calculated value (Fig. S16 in Supporting information), indicating the nearly 100% faradaic efficiency and better electrocatalytic H_2 generation performance. These results prove that the electrolysis has almost no side effects and is beneficial to the high evolution efficiency of H_2 [52]. So as to investigate the electrocatalytic robustness of the MoO_3-$PW_{12}O_{40}$ HNSs catalyst, successive CV curves have been conducted. As shown in Fig. 4e, the LSV curve of MoO_3-$PW_{12}O_{40}$ HNSs after recycling 1000 cycles shows negligible changes. Also, the chronoamperometry measurement exhibits that there is no obvious activity degradation of MoO_3-$PW_{12}O_{40}$ HNSs after continuous electrolysis for 48 h (the inset of Fig. 4e). These results verify that MoO_3-$PW_{12}O_{40}$ HNSs has good stability in the long-term electrochemical process, illustrating its potential for practical water splitting applications.

In summary, we have demonstrated that the MoO_3-POM nanobelts superstructures with abundant oxygen vacancies and highly exposed surface were successfully prepared for use as the HER catalyst *via* a simple hydrothermal method. The obtained MoO_3-$PW_{12}O_{40}$ HNSs need a low overpotential of 108 mV to achieve 10 mA/cm^2 current density in 0.5 mol/L H_2SO_4 and show the excellent long-term stability of 48 h. Its electrocatalytic HER performance is not only superior to that of corresponding MoO_3@POM bulk samples and single MoO_3, but also better than most previously reported POMs and MoO_3-based electrocatalysts. Based on experimental characterizations, the excellent HER performances of MoO_3-$PW_{12}O_{40}$ HNSs can be attributed to the following aspects: (i) The MoO_3-POM superstructure with rich oxygen vacancies and highly exposed surface provide abundant adsorption and active sites for the H* adsorption; (ii) The incorporation of POMs improved the electronic mobility and modulated the surface electronic structure of MoO_3, thus accelerating the electron transfer and optimizing the H* adsorption/desorption and dehydrogenation kinetics. This work offers a novel direction to develop metal oxide-based catalyst with high atom utilization efficiency for electrocatalytic H_2 production.

Declaration of competing interest

The authors declare that they have no known competing financial interests or personal relationships that could have appeared to influence the work reported in this paper.

CRediT authorship contribution statement

Bowen Li: Writing – original draft, Software, Methodology, Investigation, Data curation. **Ting Wang:** Writing – review & editing, Validation, Resources, Project administration, Data curation, Conceptualization. **Ming Xu:** Writing – review & editing, Supervision, Software, Resources, Project administration. **Yuqi Wang:** Validation, Software. **Zhaoxing Li:** Validation, Software. **Mei Liu:** Writing – review & editing, Supervision, Resources, Project administration. **Wenjing Zhang:** Validation, Software. **Ming Feng:** Writing – review & editing, Resources, Project administration.

Acknowledgments

This work is financially supported by the Program for the Development of Science and Technology of Jilin Province (Nos. YDZJ202201ZYTS313, YDZJ202201ZYTS395, 20240402072GH, and 20240101004JJ), and the National Natural Science Foundation of China (Nos. 22201097 and 52171210).

Supplementary materials

Supplementary material associated with this article can be found, in the online version, at doi:10.1016/j.cclet.2024.110467.

References

[1] J. Li, J. Li, J. Ren, et al., Nano-Micro Lett. 14 (2022) 148.
[2] P.D. Zhao, S.Q. Fu, L.L. Cheng, et al., Coord. Chem. Rev. 498 (2024) 215452.
[3] X.L. Cui, Y.M. Sun, X.X. Xu, Chin. Chem. Lett. 34 (2023) 107348.
[4] L. Zhang, Z.H. Hu, J.T. Huang, et al., J. Adv. Ceram. 11 (2022) 1294–1306.
[5] Y. An, L.L. Wang, W.Y. Jiang, et al., Polyoxometalates 2 (2023) 9140030.
[6] F.H. Wang, B.B. Dong, J.W. Wang, et al., J. Adv. Ceram. 11 (2022) 1208–1221.
[7] J.X. Ge, J. Hu, Y.T. Zhu, et al., Acta Phys. Chim. Sin. 36 (2020) 1906063.
[8] J.L. Zhu, J.M. Qian, X.B. Peng, et al., Nano-Micro Lett. 15 (2023) 30.
[9] C.R. Pia, C. Huang, Y.X. Yang, et al., Appl. Catal. B: Environ. 263 (2020) 118358.
[10] L.W. Xiong, Y.F. Qiu, X. Peng, et al., Nano Energy 104 (2022) 107882.
[11] X. Zhu, L.Y. Chen, Y.G. Liu, et al., Polyoxometalates 2 (2023) 9140031.
[12] X.X. Li, X.C. Liu, C. Liu, et al., Tungsten 5 (2023) 100–108.
[13] S. Feng, D.L. Li, H. Dong, et al., Appl. Catal. B: Environ. 342 (2024) 123451.
[14] D.J. Zang, Y.C. Huang, Q. Li, et al., Appl. Catal. B: Environ. 249 (2019) 163–171.
[15] M.Y. Hou, L.R. Zheng, D. Zhao, et al., Nat. Commun. 15 (2024) 1342.
[16] X. Peng, Y.J. Yan, S.J. Xiong, et al., J. Mater. Sci. Technol. 118 (2022) 136–143.
[17] Y.Y. Zhang, M.X. Chen, P. Guo, et al., Carbon Energy 5 (2023) e351.
[18] X.L. Wang, X.M. Zhang, Y.F. Xu, et al., Chem. Eng. J. 470 (2023) 144370.
[19] X. Luo, X. Tan, P.X. Ji, et al., Energy Chem. 5 (2023) 100091.
[20] G. Huang, M. Hu, X. Xu, et al., Small Struct. 4 (2023) 2200235.
[21] J.Y. Zhang, J.S. Lian, Q. Jiang, et al., Energy Environ. Sci. 15 (2022) 3945–3957.
[22] Y. Wang, X.P. Li, M.M. Zhang, et al., Adv. Mater. 34 (2022) 2107053.
[23] X. Peng, S. Xie, S.J. Xiong, et al., J. Energy Chem. 81 (2023) 574–582.
[24] J. Li, Y. Cheng, J.N. Zhang, et al., ACS Appl. Mater. Interfaces 11 (2019) 27798–27804.
[25] X.P. Li, Y. Wang, J.J. Wang, et al., Adv. Mater. 32 (2020) 2003414.
[26] F.T. Haase, A. Bergmann, T.E. Jones, et al., Nat. Energy 7 (2022) 765–773.
[27] J.L. Liu, N. Liu, H.W. Wang, et al., J. Am. Chem. Soc. 142 (2020) 17557–17563.
[28] Z. Zeb, Y.C. Huang, L.L. Chen, et al., Coord. Chem. Rev. 482 (2023) 215058.
[29] L.B. Ni, J. Gu, X.Y. Jiang, et al., Angew. Chem. Int. Ed. 62 (2023) e202306528.
[30] K. Chen, G.Y. Dai, S.Q. Liu, et al., Chin. Chem. Lett. 34 (2023) 107638.
[31] J. Gautam, K. Kannan, M.M. Meshesha, et al., J. Colloid Interface Sci. 618 (2022) 419–430.
[32] J. Gautam, Y. Liu, J. Gu, et al., Adv. Funct. Mater. 31 (2021) 2106147.
[33] R. Samanta, B.K. Manna, R. Trivedi, et al., Chem. Sci. 15 (2024) 364–378.
[34] J.S. Li, X.J. Sang, W.L. Chen, et al., ACS Appl. Mater. Interfaces 7 (2015) 13714–13721.
[35] H.Y. Li, T. Wang, M. Xu, et al., J. Alloys Compd. 987 (2024) 174199.
[36] T. Wang, M. Xu, X.H. Li, et al., Inorg. Chem. Front. 7 (2020) 1676–1684.
[37] K.H. Kim, D. Hong, M.G. Kim, et al., ACS Mater. Lett. 5 (2023) 1196–1201.
[38] X.D. Wei, Y.D. Chai, N. Liu, et al., Int. J. Hydrog. Energy 47 (2022) 9606–9615.
[39] Y.F. Liu, Y. Chen, C.M. Liang, et al., Int. J. Hydrog. Energy 51 (2024) 701–708.
[40] C.L. Li, Z.J. Zhang, R. Liu, et al., Small 16 (2020) 2003777.
[41] P. Wang, T. Wang, M. Xu, et al., Chin. Chem. Lett. 35 (2024) 108930.
[42] H.H. Luo, L.Q. Yu, K.H. Xue, et al., Sep. Purif. Technol. 330 (2024) 125373.
[43] Y.Y. Fan, Y. Gu, D.X. Wang, et al., J. Energy Chem. 95 (2024) 428–439.
[44] J.P. Chen, J.P. Zheng, W.D. He, et al., Nano Res. 16 (2023) 4603–4611.
[45] T.V. Nguyen, M. Tekalgne, T.P. Nguyen, et al., Battery Energy 2 (2023) 20220057.
[46] Y.H. Ma, D.F. Leng, X.M. Zhang, et al., Small 18 (2022) 2203173.
[47] X. Peng, S. Xie, X. Wang, et al., J. Mater. Chem. A 10 (2022) 20761.
[48] Y.H. Zheng, H.T. Hu, L. Qian, et al., J. Colloid Interface Sci. 652 (2023) 1803–1811.
[49] C. Li, H. Jang, M.G. Kim, et al., Appl. Catal. B: Environ. 307 (2022) 121204.
[50] F.H. Yuan, L.L. Ma, Z.D. Cui, et al., Rare Met. 41 (2022) 2624–2632.
[51] C.R. Pi, X.X. Li, X.M. Zhang, et al., Small 18 (2022) 2201137.
[52] B.C. Xu, Y.P. Miao, M.Q. Mao, et al., Rare Met. 43 (2024) 2660–2670.